

Bose polarons near quantum criticality

Zoe Z. Yan¹, Yiqi Ni¹, Carsten Robens¹, and Martin W. Zwierlein¹

¹MIT-Harvard Center for Ultracold Atoms, Research Laboratory of Electronics, and Department of Physics, Massachusetts Institute of Technology, Cambridge, Massachusetts 02139, USA

(Dated: September 10, 2022)

The emergence of quasiparticles in strongly interacting matter represents one of the cornerstones of modern physics. However, when different phases of matter compete near a quantum critical point, the very existence of quasiparticles comes under question. Here we create Bose polarons near quantum criticality by immersing atomic impurities in a Bose-Einstein condensate (BEC) with near-resonant interactions. Using locally-resolved radiofrequency spectroscopy, we probe the energy, spectral width, and short-range correlations of the impurities as a function of temperature. Far below the superfluid critical temperature, the impurities form well-defined quasiparticles. However, their inverse lifetime, given by their spectral width, is observed to increase linearly with temperature, a hallmark of quantum critical behavior. Close to the BEC critical temperature, the spectral width exceeds the binding energy of the impurities, signaling a breakdown of the quasiparticle picture near quantum criticality.

A great success of quantum many-body physics is the description of a large variety of strongly interacting systems by a collection of weakly interacting quasiparticles [1]. A paradigmatic example of such a quasiparticle is an electron propagating through an ionic crystal. As anticipated by Landau [2], Pekar found that the electron can create its own bound state by polarizing its environment [3, 4]. The electron dressed by lattice distortions forms a quasiparticle, which he named the *polaron*. The polaron concept [5, 6] finds wide application across condensed matter physics, in phenomena ranging from colossal magneto-resistance, to charge transport in organic semiconductors, and to high-temperature superconductivity [7]. However, near quantum phase transitions, where different phases of matter compete, the quasiparticle concept breaks down [8]. In such a quantum critical regime, where the temperature T sets the only remaining energy scale, all relaxation times become as short as allowed by quantum mechanics, *i.e.*, on the order of the Planck time $\hbar/k_B T$. The ensuing breakdown of well-defined quasiparticles appears to be at work in the “strange metal” regime of cuprate superconductors, where resistivity is found to scale linearly with temperature [9].

Ultracold quantum gases provide an ideal testing ground to study the fate of quasiparticles near quantum critical points. Species composition and densities, interaction strengths, and confining geometries can be controlled in a pristine fashion [10]. Bulk gases close to Feshbach resonances have been shown to feature a quantum critical region near the onset of quantum degeneracy, separating the dilute classical gas from superfluid or Fermi liquid states [8, 11–14]. The dressing of resonant impurities into quasiparticles in such a cold atom environment was first observed in the case of the Fermi polaron [15–21] – an atomic impurity embedded in a Fermi sea [22–24]. Impurities immersed in a Bose-Einstein condensate (BEC) have been posited to form

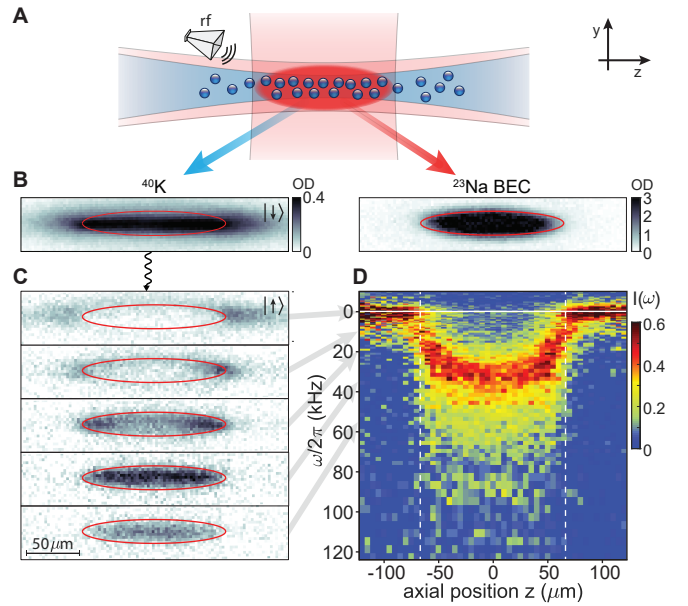


FIG. 1. Locally-resolved radiofrequency (rf) ejection spectroscopy of strongly-coupled Bose polarons for a peak interaction strength of $(k_n a)^{-1} = -0.3$. (A) Illustration of impurities (blue) immersed in a Bose-Einstein condensate (red), both trapped in a dual-color optical dipole trap. (B) *In-situ* column densities of ⁴⁰K impurities in the strongly-interacting spin state $|\downarrow\rangle$ (left) immersed in a ²³Na BEC (right), where the red ellipses mark the Thomas-Fermi boundary. (C) Impurities transferred into the non-interacting $|\uparrow\rangle$ state at various rf frequencies, as indicated by the arrows. (D) Local rf transfer $I(\omega)$ of the impurity column density as a function of axial position. The dashed vertical lines mark the condensate’s axial Thomas-Fermi radius and the solid horizontal line at $\omega/2\pi = 0$ kHz denotes the bare atomic transition.

the paradigmatic Bose polarons originally considered by Pekar [25–27]. Predicting the Bose polaron’s fate upon entering the regime of strong impurity-boson interactions has proven a challenge even at zero temperature, yielding diverging results on its properties from the ground-

state energy to the effective mass [27–34]. The complexity of describing the strongly-coupled Bose polaron increases further at non-zero temperatures [35]. In particular, in the quantum critical region near the onset of quantum degeneracy and for resonant interactions the very existence of a well-defined quasiparticle is in question [8, 12, 14]. Experimentally, evidence of Bose polaronic phenomena was observed in the expansion [36] and trapping [37] of fermions immersed in a BEC, through the phononic Lamb shift [38], and in the dynamics of impurities [39]. The continuum of excited states of impurities was probed in radiofrequency (rf) *ejection* spectroscopy [40] on Bose-Fermi mixtures [41, 42] and in a two-state mixture of bosons [43], yielding evidence for polaronic energy shifts of such excitations.

Here we create and study the strongly-coupled Bose polaron in equilibrium and explore its evolution in the approach to the quantum critical regime near the onset of quantum degeneracy of the bosonic bath. Utilizing locally-resolved *ejection* spectroscopy [40], we measure the polaron’s momentum-integrated spectral function [44], giving access to the polaron’s energy, the quasiparticle lifetime, and the strength of short-range correlations with the host bosons. These correlations are quantified by the contact [44–49], which also captures the change in the polaron energy with interaction strength. For near-resonant interactions, we find the spectral width Γ – a measure of the quasiparticle decay rate [15, 21, 44, 50] – to grow linearly with temperature, and $\hbar\Gamma$ to exceed the impurity’s energy close to the onset of quantum degeneracy for the bosonic bath. These properties of the spectral width are direct signatures of quantum critical behavior.

The experiment starts with an ultracold gas of fermionic ^{40}K atoms immersed in a BEC of ^{23}Na [36] at a temperature of $T \approx 130$ nK. Both species are trapped in an optical dipole trap as ellipsoidal atom clouds in their respective hyperfine ground states ($|F=1, m_F=1\rangle$ for ^{23}Na and $|9/2, -9/2\rangle \equiv |\downarrow\rangle$ for ^{40}K). Peak boson and fermion densities are $n_{\text{Na}} = 6 \times 10^{13} \text{ cm}^{-3}$ and $n_{\text{K}} = 2 \times 10^{11} \text{ cm}^{-3}$, corresponding to an impurity concentration of 0.3%. To create strongly-coupled Bose polarons in their attractive ground state, we ramp the magnetic field close to an interspecies Feshbach resonance [36, 40], where impurities in the $|\downarrow\rangle$ state are strongly attracted to the sodium atoms with a peak interaction strength of $(k_n a)^{-1} = -0.3$. Here, $k_n = (6\pi^2 n_{\text{Na}})^{1/3} = (1300 a_0)^{-1}$ is the inverse interboson distance, a is the interspecies scattering length, and a_0 is the Bohr radius. For these near-resonant interactions, the thermal equilibration time set by two-body collisions is near its unitarity-limited value of $\hbar/E_n \approx 4 \mu\text{s}$, three orders of magnitude faster than the lifetime of the gas mixture in this regime, limited by three-body losses to about 4 ms. Here, $E_n = \hbar^2 k_n^2 / 4m_r$ is the degeneracy energy scale, and $m_r = m_{\text{K}} m_{\text{Na}} / (m_{\text{K}} + m_{\text{Na}})$ is the re-

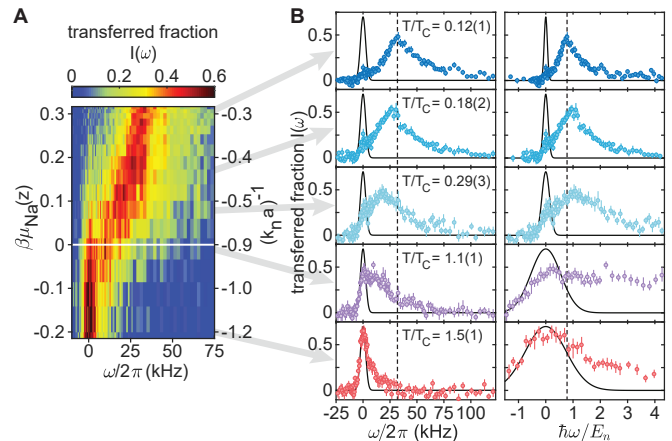


FIG. 2. Rf ejection spectra of Bose polarons at various reduced temperatures T/T_C with a peak interaction strength of $(k_n a)^{-1} = -0.3$. **(A)** Color density map of the rf transfer $I(\omega)$ as a function of the normalized local chemical potential $\beta\mu(z)$ and the local interaction strength $(k_n a)^{-1}$. The solid white line marks the BEC phase transition at $\beta\mu = 0$. **(B)** Fraction of impurities transferred into the non-interacting state $|\uparrow\rangle$ as a function of rf frequency (left) and of normalized frequency, $\hbar\omega/E_n$ (right). The dashed black line marks the peak transfer location of the impurities at the lowest T/T_C . The solid black lines show the rf spectrum of bare ^{40}K atoms, indicating the spectral resolution.

duced mass of the impurity-boson scattering problem. By preparing the strongly interacting system within 2 ms, we can study Bose polarons in equilibrium before losses take place. At the chosen magnetic field, impurities in the $|\downarrow\rangle$ state are strongly interacting with the condensate, while they are non-interacting in the hyperfine state ($|9/2, -7/2\rangle \equiv |\uparrow\rangle$). This provides us with the ideal conditions to perform rf ejection spectroscopy, whereby an rf pulse transfers impurities from the interacting $|\downarrow\rangle$ state into the non-interacting $|\uparrow\rangle$ state. We employ an rf pulse of Gaussian envelope with a full-width-half-maximum resolution of 6 kHz and measure the fraction of impurities $I(\omega)$ transferred into the $|\uparrow\rangle$ state.

Fig. 1 displays the locally-resolved rf spectrum of strongly-coupled Bose polarons. As shown in Fig. 1A, the rf transfer $I(\omega)$ is strongly spatially dependent, and its maximum is shifted furthest from the bare atomic resonance for impurities deep inside the BEC (Fig. 1B). Here, the rf photon must supply a significant additional amount of energy to transfer the bound impurity into the non-interacting state. The central peak shift in Fig. 1C corresponds to an energy shift of $\hbar \cdot 32 \text{ kHz} = 0.82 E_n$, indicating an impurity energy that is unitarity-limited, given by the degeneracy energy scale E_n . For comparison, the mean-field energy experienced by bosons in the BEC is only $\approx \hbar \cdot 0.8 \text{ kHz}$. In addition to the strong shift, we also observe long tails at higher frequencies in the rf transfer, a tell-tale sign of contact interactions [45, 46, 51].

Interpreting the spatially-resolved spectrum under

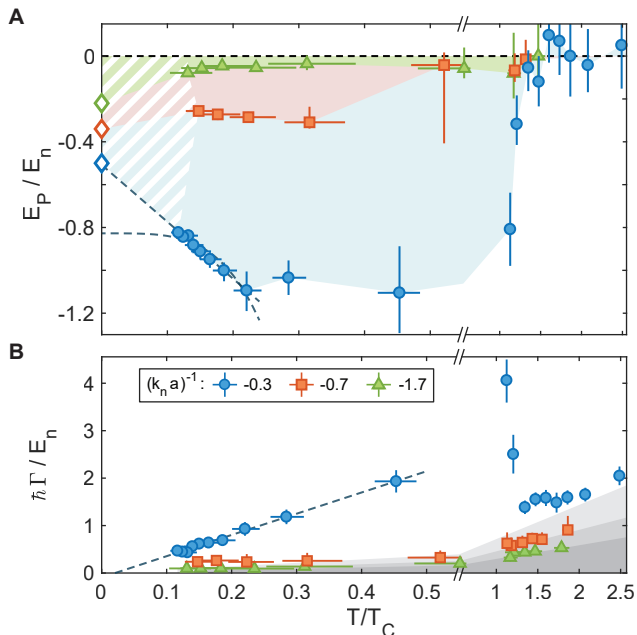


FIG. 3. Evolution of the Bose polaron as a function of the local reduced temperature T/T_C for various peak interaction strengths $(k_n a)^{-1}$. **(A)** Energy of the Bose polaron. The shaded areas are a guide to the eye and the blue dashed lines represent linear and quartic extrapolations to zero temperature. The prediction of the lowest-order T-matrix calculation is represented by open diamonds at $T=0$. **(B)** The inverse lifetime of the Bose polaron, represented by the half-width at half-maximum (Γ) of the local rf spectra [40]. The grey shaded areas indicate the spectral resolutions of the corresponding rf pulses. The dashed line is a linear fit to the data below T_C .

the assumption of the local density approximation (LDA) [40, 52] gives access to the rf spectrum of the impurity as a function of the condensate's local chemical potential $\mu(z) = \mu_0 - V_{Na}(z)$. Here, $\mu_0 = 4\pi\hbar^2 a_{BB} n_{Na}/m_{Na}$ is the condensate's chemical potential at its peak density, $a_{BB} = 52 a_0$ the scattering length between bosons [53], and $V_{Na}(z)$ is the radially-centered trapping potential along the axial direction. Fig. 2A shows the rf spectrum as a function of $\beta\mu(z)$, the chemical potential normalized by $\beta = 1/k_B T$. The interaction parameter $(k_n a)^{-1}$ also varies with the local density $n_{Na}(z)$ as indicated. A strong shift of the rf transfer for positive chemical potentials is clearly visible. Fig. 2B shows a selection of spectra, indicating the temperature T normalized by the local critical temperature $T_C(z) = 0.31 \frac{\hbar^2}{k_B m_{Na}} (n_{Na}(z))^{2/3}$ for a homogeneous gas. The absolute frequency of the spectral peak continuously decreases with higher reduced temperatures (left panel). However, when normalized by the degeneracy energy scale E_n , the spectral peak frequency in fact increases, indicating a more strongly-bound impurity with increasing temperatures up to the critical temperature T_C (right panel). This finding is summa-

rized in Fig. 3A, where the peak frequency shift ω_p is interpreted as the ground-state energy $E_p = -\hbar\omega_p$ of the Bose polaron [40]. Stronger binding of the impurity to the bosonic bath with increasing temperature has been predicted [35]. Additionally, a broadening of the spectral function underlying the rf spectrum may contribute to the observed shift [21]. Above T_C the peak energy shift suddenly jumps to zero, despite the near-unitarity-limited interactions. This behavior is expected when the temperature exceeds the energy difference between the attractive and repulsive branches of the resonantly interacting impurity, which occurs near the onset of quantum degeneracy [54, 55]. A similar jump in binding energy was recently observed for an impurity resonantly interacting with a nearly degenerate Fermi gas [21]. At weaker interaction strengths, away from the quantum critical regime, we observe that the Bose polaron is less strongly bound to the bath, as expected (see Fig. 3A).

In the strongly interacting regime where $(k_n a) \gg 1$, our measurements probe a regime where the binding energy is much larger than the condensate's local mean-field energy. In this regime, a universal description for the Bose polaron at low temperatures emerges from a lowest order T-matrix and an equivalent variational approach [28, 40, 56]: here, the impurity acquires an energy shift that is the sum of the individual and uncorrelated shifts from each host boson:

$$E_p \equiv -\frac{\hbar^2 \kappa^2}{2m_r} = -\frac{2\pi\hbar^2 n_{Na}}{m_r} f(i\kappa) \quad (1)$$

where $f(i\kappa) = -\frac{a}{1-\kappa a}$ is the two-body scattering amplitude evaluated at imaginary momentum $i\kappa$, as appropriate for a bound state. The equation implicitly gives E_p , whose natural energy scale is confirmed as the degeneracy energy scale E_n for an effective particle of reduced mass m_r and density n_{Na} . In this scenario, E_p/E_n is a universal function of $(k_n a)^{-1}$ only. For weak attractive impurity-boson interactions ($(k_n a)^{-1} \ll -1$) one finds the mean-field result $E_p = 2\pi\hbar^2 n_{Na} a/m_r$, while on the molecular side of the Feshbach resonance in the limit $(k_n a)^{-1} \gg 1$, the polaron energy becomes equal to the energy of a two-body molecule of size a , $E_p = -\frac{\hbar^2}{2m_r a^2}$. On resonance, the approach yields $E_p/E_n = -0.71$, which is similar to the result for the unitary Fermi polaron, $E_p/E_n = -0.61$ [22, 57]. The Bose polaron is more strongly bound than its fermionic counterpart due to the lack of constraints imposed by Pauli exclusion [40]. The polaron energies according to the T-matrix approach for $T=0$ are indicated as open diamonds in Fig. 3A. A linear extrapolation to zero temperature of our strong-coupling binding energy data appears to agree well with this theory. Alternatively, assuming the increase in binding strength with temperature is due to coupling to the BEC's finite temperature phonon bath, one may attempt a T^4 fit to the data [58]. Both the linear and quartic extrapolations exclude a simple mean-field prediction that

yields $E_p/E_n = -1.4$ for $(k_n a)^{-1} = -0.3$.

The binding energy alone does not reveal whether the impurities in the bosonic bath form well-defined quasiparticles. This also requires knowledge of the impurities' spectral width, a measure of the quasiparticle's decay rate [15, 21, 44, 50]. Generally, the width of an rf spectrum corresponds to the rate at which the coherent evolution of an atomic spin is interrupted during the rf pulse. For quasiparticles, it is momentum-changing collisions with host bosons that cause such decoherence, the same process that limits the quasiparticle's lifetime. The rf spectral width thus directly measures the inverse lifetime of the quasiparticles [15, 21, 44, 50]. Fig. 3B shows that at the strongest interactions the impurity's spectral width follows a striking linear dependence with temperature: $\Gamma = 8.1(5) k_B T/\hbar$. The observed trend suggests a well-defined quasiparticle with vanishing spectral width in the limit of zero temperature. However, near T_C , the rf spectral width increases significantly beyond the measured binding energy E_p , signaling a breakdown of the quasiparticle picture. We attribute both the linear temperature dependence and the quasiparticle breakdown to the system's vicinity to the quantum critical regime near the onset of quantum degeneracy at $\mu \rightarrow 0$ and resonant interactions at $(k_n a)^{-1} \rightarrow 0$. Here, as only one relevant energy scale remains ($k_B T \sim k_B T_C = 0.55 E_n$ [59]), the spectral width also scales as $k_B T/\hbar$ and no quasiparticles are predicted to persist [8, 11]. In this regime, the impurities have the shortest mean-free path possible with contact interactions, *i.e.*, one interboson distance. We do not observe similar signs of quantum criticality at lower interaction strengths, where the spectral widths become much narrower than the scale set by temperature $k_B T/\hbar$ (see Fig. 3B).

Spectra obtained via rf ejection spectroscopy encode the wavefunction overlap between the interacting, dressed impurity and a non-interacting state. As such, they not only contain information about the binding energy and lifetime of the impurity, but also about the short-range correlations between the impurity and the surrounding medium. Indeed, the final state of an ejection spectrum at high rf frequencies is a free impurity with large momentum $\hbar k$. Hence, high frequencies in ejection spectroscopy probe the initial wavefunction at short distances [45, 46, 48, 49]. This leads to characteristic tails $\propto \omega^{-3/2}$ of the rf spectra, reflecting the two-body nature of the wavefunction at short distances. The strength of the rf transfer is directly proportional to the contact C , a thermodynamic quantity describing the probability that the impurity is in close vicinity to the host bosons. Through the Hellmann-Feynman theorem, the contact is also equal to the change in energy with the inverse impurity-boson scattering length: $\frac{C}{k_n} = 2\pi \frac{d}{d(k_n a)^{-1}} \left(\frac{-E_p}{E_n} \right)$ [45–47, 49]. The high-frequency

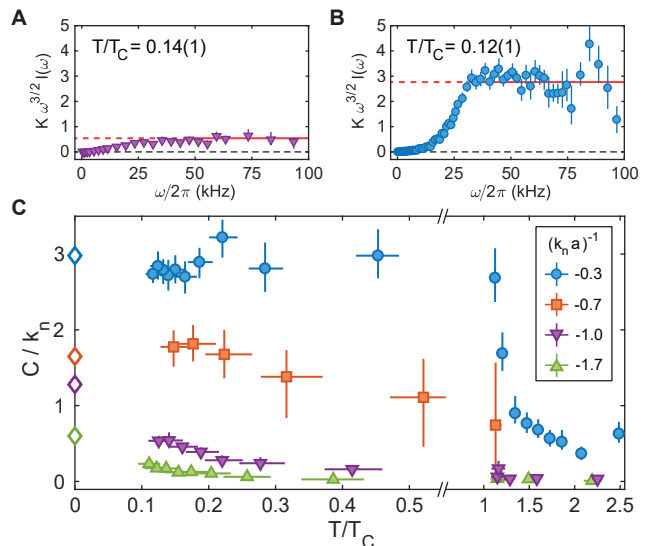


FIG. 4. Contact of the Bose polaron. The low temperature rf transfer for (A) $(k_n a)^{-1} = -1$ and (B) $(k_n a)^{-1} = -0.3$ multiplied by $K\omega^{3/2}$, with $K = \frac{8\sqrt{2\pi m_r}}{\Omega_P^2 \sigma \sqrt{\hbar}} \frac{1}{k_n}$, displays a plateau that yields the normalized contact C/k_n . The contact is obtained from fits in the frequency region indicated by the solid red line. (C) The contact, normalized by k_n , as a function of the reduced temperature at various interaction strengths. The open diamonds at $T=0$ are the T-matrix predictions from Eq. 3.

tail of the rf transfer $I(\omega)$ can be written [48]:

$$I(\omega) \underset{\omega \rightarrow \infty}{=} \frac{\Omega_P^2 \sigma}{8} \sqrt{\frac{\hbar}{2\pi m_r}} \frac{C}{\omega^{3/2}} \quad (2)$$

where σ is the Gaussian $e^{-1/2}$ width of the rf pulse's duration and Ω_P the peak Rabi frequency [40]. Our spectra follow this behavior closely: when multiplied by $\omega^{3/2}$, they asymptote to plateaus that yield the contact's value, shown for $(k_n a)^{-1} = -1$ in Fig. 4A and $(k_n a)^{-1} = -0.3$ in Fig. 4B, respectively. Fig. 4C summarizes our measurements of the contact, normalized by k_n , as a function of T/T_C for various interaction strengths. From weak to strong attractive interactions, the contact increases monotonically. For the strongest interaction strength the normalized contact remains approximately constant for all values $T/T_C < 1$. An abrupt drop of the normalized contact is seen above the BEC transition temperature, though it remains non-zero. This is expected for a Boltzmann gas with unitarity-limited interactions that has a non-zero contact given by the inverse mean-free path, $n\sigma \propto 1/T$. Therefore C/k_n decreases as T_C/T in the non-degenerate regime [21, 55]. The low-temperature value of the normalized contact is close to what one finds for the unitary Fermi polaron ($C/k_n = 4.3$ [21]), the balanced unitary Fermi gas [60–62], and the near-unitary BEC [63]. Using the variational ansatz for the Bose polaron's energy (see Eq. 1), we obtain an expression for the

normalized contact:

$$\frac{C}{k_n} = \pi^2 \frac{E_p/E_n}{E_n/E_p - \frac{\pi}{4} \frac{1}{k_n a}} \quad (3)$$

which yields $\frac{C}{k_n} = \pi^2 \left(\frac{E_p}{E_n}\right)^2 = 5.0$ on resonance. The contact can also be interpreted in an intuitive picture [47]: it gives the number of bosons $N_B(s)$ within a sphere of radius s around the impurity: $N_B(s) = Cs/4\pi$ for $s \ll n_{\text{Na}}^{-1/3}$ and $s \ll |a|$. The measured near-unity value of $C/4\pi$ in units of the interboson spacing thus indicates that even for near-unitarity-limited interactions – on average – only about one extra boson is in close proximity to the impurity. In this respect, the resonant Bose polaron shares traits with a molecular dimer of a size given by the interboson distance. Within the variational description, the localized part of the polaron’s wavefunction is of identical form to that of a molecule, and away from resonance where $a > 0$, the polaron smoothly evolves into a molecule of size a [28, 40, 56].

For future studies, it will be interesting to probe transport properties of the impurities and specifically investigate whether their resistivity scales linearly with temperature, in analogy to findings in the strange metal phase of the cuprates [9]. Furthermore, increasing the impurity concentration might allow the formation of bipolarons [64] and the observation of phonon-induced superfluidity [65, 66].

The authors thank Richard Schmidt, Fabian Grusdt, Yulia Shchadilova, Kushal Seetharam, Eugene Demler, Eberhard Tiemann, and Wilhelm Zwerger for useful discussions. We also thank Joris Verstraten, Alexander Chuang, and Elisa Soave for experimental assistance. This work was supported by the NSF, AFOSR, ARO, an AFOSR MURI on “Exotic Phases of Matter”, the David and Lucile Packard Foundation, and the Gordon and Betty Moore Foundation through grant GBMF5279. Z. Z. Y. acknowledges support from the NSF GRFP.

[1] P. Nozieres and D. Pines, *The Theory of Quantum Liquids* (Perseus Books, Cambridge, 1999).
 [2] L. D. Landau, Phys. Z. Sowjetunion **3**, 644 (1933).
 [3] S. I. Pekar, Zh. Eksp. Teor. Fiz. **16**, 335 (1946). *English translation in Journal of Physics USSR*, **10**, 341 (1946).
 [4] S. I. Pekar, Zh. Eksp. Teor. Fiz. **16**, 341 (1946). *English translation in Journal of Physics USSR*, **10**, 347 (1946).
 [5] H. Fröhlich, Adv. Phys. **3**, 325 (1954).
 [6] R. P. Feynman, Phys. Rev. **97**, 660 (1955).
 [7] A. S. Alexandrov and J. T. Devreese, *Advances in Polaron Physics*, Vol. 159 (Springer-Verlag, Berlin, 2010).
 [8] S. Sachdev, *Quantum Phase Transitions*, 2nd ed. (Cambridge University Press, 2011).
 [9] P. A. Lee, N. Nagaosa, and X.-G. Wen, Rev. Mod. Phys. **78**, 17 (2006).

[10] I. Bloch, J. Dalibard, and W. Zwerger, Rev. Mod. Phys. **80**, 885 (2008).
 [11] P. Nikolić and S. Sachdev, Phys. Rev. A **75**, 033608 (2007).
 [12] D. Ludwig, S. Floerchinger, S. Moroz, and C. Wetterich, Phys. Rev. A **84**, 033629 (2011).
 [13] T. Enss, Phys. Rev. A **86**, 013616 (2012).
 [14] G. Bertaina, E. Fratini, S. Giorgini, and P. Pieri, Phys. Rev. Lett. **110**, 115303 (2013).
 [15] A. Schirotzek, C. H. Wu, A. Sommer, and M. W. Zwierlein, Phys. Rev. Lett. **102**, 230402 (2009).
 [16] S. Nascimbène, N. Navon, K. J. Jiang, L. Tarruell, M. Teichmann, J. McKeever, F. Chevy, and C. Salomon, Phys. Rev. Lett. **103**, 170402 (2009).
 [17] M. Koschorreck, D. Pertot, E. Vogt, B. Fröhlich, M. Feld, and M. Köhl, Nature **485**, 619 (2012).
 [18] C. Kohstall, M. Zaccanti, M. Jag, A. Trenkwalder, P. Massignan, G. M. Bruun, F. Schreck, and R. Grimm, Nature **485**, 615 (2012).
 [19] M. Cetina, M. Jag, R. S. Lous, I. Fritsche, J. T. Walraven, R. Grimm, J. Levinsen, M. M. Parish, R. Schmidt, M. Knap, and E. Demler, Science **354**, 96 (2016).
 [20] F. Scazza, G. Valtolina, P. Massignan, A. Recati, A. Amico, A. Burchianti, C. Fort, M. Inguscio, M. Zaccanti, and G. Roati, Phys. Rev. Lett. **118**, 083602 (2017).
 [21] Z. Yan, P. B. Patel, B. Mukherjee, R. J. Fletcher, J. Struck, and M. W. Zwierlein, Phys. Rev. Lett. **122**, 093401 (2019).
 [22] F. Chevy, Phys. Rev. A **74**, 063628 (2006).
 [23] N. Prokof’ev and B. Svistunov, Phys. Rev. B **77**, 020408 (2008).
 [24] R. Schmidt, M. Knap, D. A. Ivanov, J. S. You, M. Cetina, and E. Demler, Reports Prog. Phys. **81**, 024401 (2018).
 [25] R. M. Kalas and D. Blume, Phys. Rev. A **73**, 043608 (2006).
 [26] F. M. Cucchietti and E. Timmermans, Phys. Rev. Lett. **96**, 210401 (2006).
 [27] J. Tempere, W. Casteels, M. K. Oberthaler, S. Knoop, E. Timmermans, and J. T. Devreese, Phys. Rev. B **80**, 184504 (2009).
 [28] S. P. Rath and R. Schmidt, Phys. Rev. A **88**, 053632 (2013).
 [29] R. S. Christensen, J. Levinsen, and G. M. Bruun, Phys. Rev. Lett. **115**, 160401 (2015).
 [30] F. Grusdt, Y. E. Shchadilova, A. N. Rubtsov, and E. Demler, Sci. Rep. **5** (2015).
 [31] J. Vlietinck, W. Casteels, K. V. Houcke, J. Tempere, J. Ryckebusch, and J. T. Devreese, New Journal of Physics **17**, 033023 (2015).
 [32] F. Grusdt and M. Fleischhauer, Phys. Rev. Lett. **116**, 053602 (2016).
 [33] Y. E. Shchadilova, R. Schmidt, F. Grusdt, and E. Demler, Phys. Rev. Lett. **117**, 113002 (2016).
 [34] S. M. Yoshida, S. Endo, J. Levinsen, and M. M. Parish, Phys. Rev. X **8**, 011024 (2018).
 [35] N. E. Guenther, P. Massignan, M. Lewenstein, and G. M. Bruun, Phys. Rev. Lett. **120**, 050405 (2018).
 [36] J. W. Park, C.-H. Wu, I. Santiago, T. G. Tiecke, S. Will, P. Ahmadi, and M. W. Zwierlein, Phys. Rev. A **85**, 051602 (2012).
 [37] B. J. DeSalvo, K. Patel, J. Johansen, and C. Chin, Phys. Rev. Lett. **119**, 233401 (2017).
 [38] T. Rentrop, A. Trautmann, F. A. Olivares, F. Jendrzejewski, A. Komnik, and M. K. Oberthaler, Phys. Rev.

- X **6**, 041041 (2016).
- [39] J. Catani, G. Lamporesi, D. Naik, M. Gring, M. Inguscio, F. Minardi, A. Kantian, and T. Giamarchi, *Phys. Rev. A* **85**, 023623 (2012).
- [40] See supplemental material.
- [41] C. H. Wu, J. W. Park, P. Ahmadi, S. Will, and M. W. Zwierlein, *Phys. Rev. Lett.* **109**, 085301 (2012).
- [42] M.-G. Hu, M. J. Van de Graaff, D. Kedar, J. P. Corson, E. A. Cornell, and D. S. Jin, *Phys. Rev. Lett.* **117**, 055301 (2016).
- [43] N. B. Jørgensen, L. Wacker, K. T. Skalmstang, M. M. Parish, J. Levinsen, R. S. Christensen, G. M. Bruun, and J. J. Arlt, *Phys. Rev. Lett.* **117**, 055302 (2016).
- [44] W. Zwerger, in *Proceedings of the International School of Physics "Enrico Fermi"*, Vol. 191, edited by M. Inguscio, W. Ketterle, S. Stringari, and G. Roati (IOP Press Books, Amsterdam, 2016) Chap. 2.
- [45] G. Baym, C. J. Pethick, Z. Yu, and M. W. Zwierlein, *Phys. Rev. Lett.* **99**, 190407 (2007).
- [46] M. Punk and W. Zwerger, *Phys. Rev. Lett.* **99**, 170404 (2007).
- [47] S. Tan, *Ann. Phys. (N. Y.)* **323**, 2952 (2008).
- [48] E. Braaten, D. Kang, and L. Platter, *Phys. Rev. Lett.* **104**, 223004 (2010).
- [49] M. W. Zwierlein, in *Proceedings of the International School of Physics "Enrico Fermi"*, Vol. 191, edited by M. Inguscio, W. Ketterle, S. Stringari, and G. Roati (IOP Press Books, Amsterdam, 2016) Chap. 3.
- [50] W. Schneider, V. B. Shenoy, and M. Randeria, (2009), arXiv:0903.3006v1.
- [51] E. Braaten and L. Platter, *Phys. Rev. Lett.* **100**, 205301 (2008).
- [52] W. Ketterle and M. W. Zwierlein, in *Making, probing, and understanding ultracold Fermi gases*, Vol. 31 (*Rivista del Nuovo Cimento*, 2008) p. 247.
- [53] E. Tiesinga, C. J. Williams, P. S. Julienne, K. M. Jones, P. D. Lett, and W. D. Phillips, *J. Res. Natl. Inst. Stand. Technol.* **101**, 505 (1996).
- [54] T.-l. Ho and E. J. Mueller, *Phys. Rev. Lett.* **92**, 160404 (2004).
- [55] R. J. Fletcher, R. Lopes, J. Man, N. Navon, R. P. Smith, M. W. Zwierlein, and Z. Hadzibabic, *Science* **355**, 377 (2017).
- [56] W. Li and S. Das Sarma, *Phys. Rev. A* **90**, 013618 (2014).
- [57] R. Combescot, A. Recati, C. Lobo, and F. Chevy, *Phys. Rev. Lett.* **98**, 180402 (2007).
- [58] J. Levinsen, M. M. Parish, R. S. Christensen, J. J. Arlt, and G. M. Bruun, *Phys. Rev. A* **96**, 063622 (2017).
- [59] Efimov trimers are not expected to enter in the description of our system at quantum criticality, as their size is predicted to be orders of magnitude larger than the interparticle spacing at our densities (see [34]).
- [60] M. G. Lingham, K. Fenech, T. Peppler, S. Hoinka, P. Dyke, P. Hannaford, and C. J. Vale, *J. Mod. Opt.* **63**, 1783 (2016).
- [61] B. Mukherjee, P. B. Patel, Z. Yan, R. J. Fletcher, J. Struck, and M. W. Zwierlein, (2019), arXiv:1902.08548.
- [62] C. Carcy, S. Hoinka, M. G. Lingham, P. Dyke, C. C. N. Kuhn, H. Hu, and C. J. Vale, (2019), arXiv:1902.07853v1.
- [63] R. J. Wild, P. Makotyn, J. M. Pino, E. A. Cornell, and D. S. Jin, *Phys. Rev. Lett.* **108**, 145305 (2012).
- [64] A. Camacho-Guardian, L. A. Peña Ardila, T. Pohl, and G. M. Bruun, *Phys. Rev. Lett.* **121**, 013401 (2018).
- [65] D. V. Eftremov and L. Viverit, *Phys. Rev. B* **65**, 134519 (2002).
- [66] J. J. Kinnunen, Z. Wu, and G. M. Bruun, *Phys. Rev. Lett.* **121**, 253402 (2018).
- [67] K. M. O'Hara, S. L. Hemmer, S. R. Granade, M. E. Gehm, J. E. Thomas, V. Venturi, E. Tiesinga, and C. J. Williams, *Phys. Rev. A* **66**, 041401 (2002).
- [68] Z. Z. Yan, "A heavy impurity immersed in a bose-einstein condensate," (2018), 49th Annual Meeting of the APS Division of Atomic, Molecular and Optical Physics APS Meeting.
- [69] L. A. P. Ardila, N. B. Jørgensen, T. Pohl, S. Giorgini, G. M. Bruun, and J. J. Arlt, (2018), arXiv:1812.04609 [cond-mat.quant-gas].
- [70] M. Naraschewski and D. M. Stamper-Kurn, *Phys. Rev. A* **58**, 2423 (1998).
- [71] F. Dalfovo, S. Giorgini, L. P. Pitaevskii, and S. Stringari, *Rev. Mod. Phys.* **71**, 463 (1998).
- [72] C. Chin and P. S. Julienne, *Phys. Rev. A* **71**, 012713 (2005).
- [73] G.D. Mahan, *Many-particle physics* (Springer Science+Business Media New York, New York, 2000).
- [74] T. L. Ho and Q. Zhou, *Nat. Phys.* **6**, 131 (2010).
- [75] M. G. Lingham, K. Fenech, S. Hoinka, and C. J. Vale, *Phys. Rev. Lett.* **112**, 100404 (2014).

Supplementary material: Bose polarons near quantum criticality

Zoe Z. Yan¹, Yiqi Ni¹, Carsten Robens¹, and Martin W. Zwierlein¹

¹*MIT-Harvard Center for Ultracold Atoms, Research Laboratory of Electronics, and Department of Physics, Massachusetts Institute of Technology, Cambridge, Massachusetts 02139, USA*

Experimental setup

The preparation of the ultracold mixture of ²³Na and ⁴⁰K closely follows the process described in [36]. In brief, the ⁴⁰K impurities and the bosonic ²³Na are cooled and trapped in a crossed optical dipole trap with wavelength $\lambda = 1064$ nm. The Na trap frequencies are (110, 78, 13) Hz in the x-, y-, and z-directions. The atoms are prepared in $|F, m_F\rangle = |1, 1\rangle$ and $|9/2, -9/2\rangle$ for ²³Na and ⁴⁰K, respectively. F is the total angular quantum number and m_F is its projection along the magnetic field axis. After evaporative cooling in the optical trap, the ²³Na cloud of $\approx 10^6$ atoms has undergone Bose-Einstein condensation and sympathetically cooled the impurities to a final temperature of 130 nK. We adiabatically ramp on an additional single-beam optical dipole trap at $\lambda = 775$ nm along the laboratory z -axis (the axial coordinate described in the main text), which provides additional confinement for the impurities but not the bosonic atoms due to their differing ac polarizabilities. This species-selective optical dipole trap cancels the differential gravitational sag between the two species. The impurity atoms form a cloud with Gaussian widths of (9, 9, 70) μm in the x-, y-, and z-axes, respectively. To tune interactions between the impurities and the bath, we make use of the Feshbach resonances between ²³Na and ⁴⁰K, shown in Fig. S1. Our previous measurement of the interspecies resonances using Feshbach loss spectroscopy was reported in [36]. For this study we refined the location of the resonances and zero-crossing of the scattering length using a technique based on interspecies thermalization (similar to the method in [67]).

In preparation for spectroscopy, we ramp the magnetic field to the vicinity of a Feshbach resonance, where the impurity-bath interaction can be tuned from weakly-to strongly-attractive. For the measurements performed with near-unity-limited interactions at $a = -3900 a_0$ (cf. Figs. 1–4 in the main text), the final magnetic field is 93.2 G, where the final state $|\uparrow\rangle$ has zero interaction with the bosons. For the data at scattering lengths $a = -840, -1800 a_0$ in the initial state (cf. Figs. 3–4 in the main text), the field is varied around a Feshbach resonance near 78.4 G, where the final state is weakly interacting ($a_{\uparrow} \approx -100 a_0$).

For ejection spectroscopy, we use an rf pulse to transfer the impurities out of the interacting state $|\downarrow\rangle$ into a non-interacting state $|\uparrow\rangle$. The Gaussian rf pulse is symmetrically

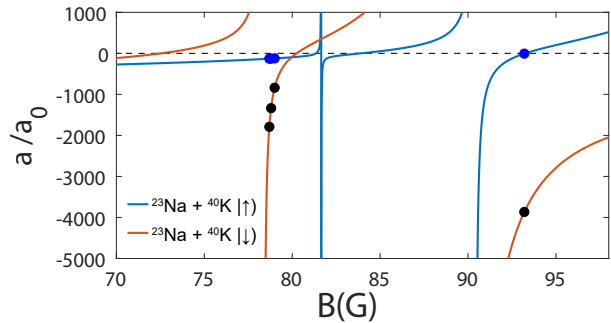


FIG. S1. The impurity-bose s-wave scattering lengths versus magnetic field for the two impurity spin states $|\uparrow\rangle, |\downarrow\rangle$. Markers denote the magnetic fields where we perform rf spectroscopy for various a (black circles), taking care to keep the magnitude of a_{\uparrow} small (blue circles). At 93.2 G we exploit the zero-crossing of the $|\uparrow\rangle$ state to avoid any final state interactions.

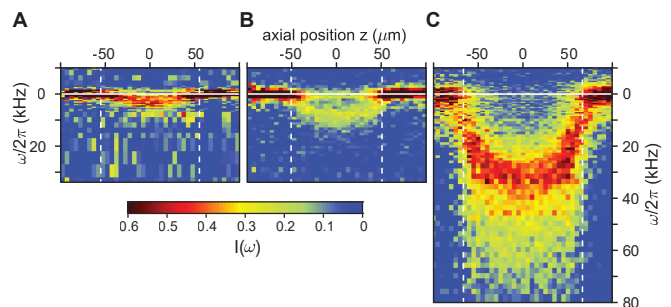


FIG. S2. Color density maps of the impurity transfer $I(\omega)$ versus rf frequency and cloud axial location, with the boson Thomas-Fermi radii denoted by the white dashed lines, for scattering lengths of (A) $-840 a_0$, (B) $-1800 a_0$, and (C) $-3900 a_0$. These scattering lengths correspond to peak interaction strengths $(k_n a)^{-1} = -1.7, -0.7$, and -0.3 , respectively, at the cloud center. In all cases, the rf drive was a Gaussian pulse lasting 500 μs , with the Gaussian $\sigma = 62.5 \mu\text{s}$. The peak Rabi frequencies on the bare atomic lines were $2\pi \times 3.5$ kHz for (a)-(b) and $2\pi \times 11$ kHz for (c).

cally truncated after a duration of 8σ , where $\sigma = 62.5 \mu\text{s}$ is the temporal $e^{-1/2}$ width of the Gaussian pulse. The spectral resolution of our pulse is dominated by Fourier broadening, leading to a pulse full-width-half-maximum (FWHM) of ≈ 6 kHz. After the rf probe, we immediately image the two impurity states and the bosons, employing *in situ* absorption imaging. Sample spectra for three

different interaction strengths are shown in Fig. S2. As described in the main text, the stronger impurity-bath couplings correspond to a greater shift in E_p .

Comparison between ejection and injection rf spectroscopy

There are two commonly used techniques to gain information on a cold-atom system using rf spectroscopy. The many-body system can be prepared by initializing the impurities in the non-interacting state and injecting them into the interacting state, a technique known as *injection* or indirect rf spectroscopy. This method has been employed [42, 43] to measure the continuum of excited polaron states. Alternatively, we can prepare the many-body system in the interacting state in thermal equilibrium and then eject the impurities out of this state (*ejection* or direct rf spectroscopy). As we will demonstrate in the following, the two techniques lead to different spectral responses: the former method excites the impurity into a continuum of states while the latter probes the impurity's ground state.

We compare the two methods at an interaction strength of $-3900 a_0$, as shown in Fig. S3. In the ejection method we employ for the data shown in the main text, the polaron is prepared in equilibrium and ejected into a non-interacting spin state, denoted $|\uparrow\rangle$. The injection method is also performed with all other parameters (*i.e.* density, rf pulse profile) held constant. As shown in Fig. S3(B), in the injection protocol, the maximum transfer of population occurs at a normalized energy of $0.2 E_n$, much lower compared to the measured energy shift of $0.8 E_n$ obtained from ejection spectroscopy. Thus, assigning the spectral peak of $0.2 E_n$ as the polaron binding energy would be a significant under-prediction. It is the onset and not the peak of the injection spectrum that encodes any meaning for the ground state polaron energy E_p [68, 69]. Moreover, only the ejection method can recover additional equilibrium quantities of the Bose polaron, including its lifetime and short-range correlations, as the injection spectrum convolves the spectral response of a continuum of excited polaron states [69].

Local boson density and reduced temperature

The *in-situ* local boson density $n_{\text{Na}}(\mathbf{r})$ – the sum of the condensate density $n_c(\mathbf{r})$ and the thermal density $n_t(\mathbf{r})$ – has the following form under the local density approximation (LDA) and the Thomas-Fermi limit [70]:

$$n_c(\mathbf{r}) = \frac{15N_c}{8\pi R_x R_y R_z} \max\left(1 - \frac{x^2}{R_x^2} - \frac{y^2}{R_y^2} - \frac{z^2}{R_z^2}, 0\right) \quad (4)$$

$$n_t(\mathbf{r}) = \frac{1}{\lambda_{\text{dB}}^3} g_{3/2}\left(\exp\left(-\beta\left[\mu_0 - \frac{1}{2}m_{\text{Na}} \sum_{i=x,y,z} \omega_i^2 r_i^2\right]\right)\right) \quad (5)$$

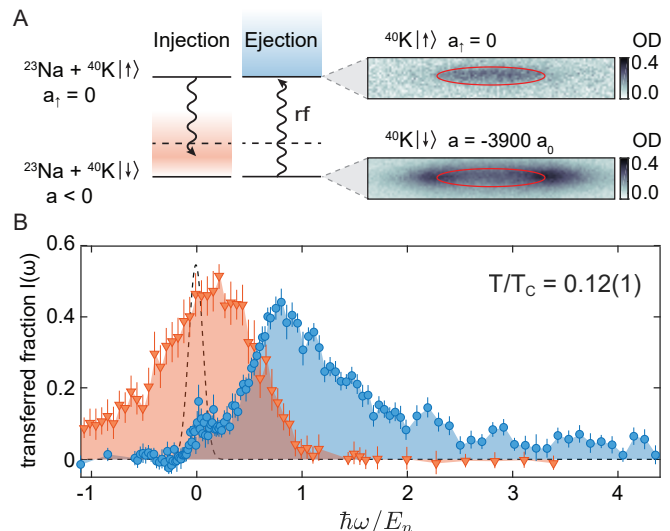


FIG. S3. Spectral response of ^{40}K impurities using ejection and injection spectroscopy. **(A)** The energy levels of the many-body system (left). The dashed lines denote the impurity's hyperfine energies and the solid lines denote the ground state polaron energies. In the ejection technique, the polaron ground state is prepared and ejected out (pictured on the bottom right as an absorption image of K in $|\downarrow\rangle$) via an rf drive to the non-interacting state $|\uparrow\rangle$ (pictured on the top right.) The BEC's Thomas-Fermi radius is marked by the red line. **(B)** A comparison of the injection and ejection lineshapes at $a = -3900 a_0$, in red and blue respectively, with peak interaction strength $(k_n a)^{-1} = -0.3$. The transfer from the initial to the final spin state is shown as a function of normalized rf frequency. The dotted black line shows the Gaussian response of the bare impurity state.

where $\lambda_{\text{dB}} = \sqrt{2\pi\hbar^2/m_{\text{Na}}k_B T}$ is the thermal de Broglie wavelength, g the Polylogarithm function, $\beta \equiv 1/k_B T$, and μ_0 the peak boson chemical potential. R_i is the Thomas-Fermi radius along the i th coordinate, defined by $\mu_0 = m\omega_i^2 R_i^2/2$. The condensate number is $N_c = \frac{8\pi}{15g_{\text{BB}}}\mu_0 R_x R_y R_z$, where $g_{\text{BB}} = 4\pi\hbar^2 a_{\text{BB}}/m_{\text{Na}}$ is the bose-bose coupling constant. The condensate is assumed to only experience mean-field repulsion, while the thermal atoms are an ideal gas confined in the external harmonic trap and the mean-field repulsion of the condensate [70]. Experimental values of μ_0 are derived from the speed of the BEC's hydrodynamic expansion after releasing the cloud in time-of-flight [71]. Temperature is also measured in time-of-flight by fitting the outer wings to the thermal density distribution. From the local density, we compute the local critical temperature T_c , where $k_B T_c(\mathbf{r}) = \frac{3.31\hbar^2}{m_{\text{Na}}} n_{\text{Na}}(\mathbf{r})^{2/3}$.

Bose Polaron properties at $T = 0$ within the variational approach

Here we obtain the Bose polaron energy and contact from a simple variational ansatz, introduced originally for the description of the Fermi polaron [22]. We work in the

limit of weak boson-boson interaction, justified *a posteriori* as we find that the boson chemical potential is much smaller than the polaron energy E_p . In this limit, the linear portion of the Bogoliubov spectrum for the bosons at low momenta is not relevant for the energetics of the polaron, and we can simply work with a free-particle dispersion. Our solution turns out to be identical to what is obtained from the lowest-order T-matrix calculation in the same limit [28].

The Hamiltonian describing the impurity interacting with the Bose gas is

$$H = \sum_{\mathbf{k}} \left(\epsilon_{B,\mathbf{k}} a_{\mathbf{k}}^\dagger a_{\mathbf{k}} + \epsilon_{I,\mathbf{k}} c_{\mathbf{k}}^\dagger c_{\mathbf{k}} \right) + \frac{g_0}{V} \sum_{\mathbf{k}\mathbf{k}'\mathbf{q}} a_{\mathbf{k}+\mathbf{q}}^\dagger c_{\mathbf{k}'-\mathbf{q}}^\dagger c_{\mathbf{k}'} a_{\mathbf{k}}. \quad (6)$$

Here, $\epsilon_{B,\mathbf{k}} = \hbar^2 k^2 / 2m_B$ and $\epsilon_{I,\mathbf{k}} = \hbar^2 k^2 / 2m_I$ are the boson and impurity free dispersions, m_B and m_I the boson and impurity mass, respectively, $a_{\mathbf{k}}^\dagger$ and $c_{\mathbf{k}}^\dagger$ are the boson and impurity creation operators, and V the quantization volume. g_0 is the bare impurity-boson coupling constant, related to the impurity-boson scattering length a via the Lippmann-Schwinger equation

$$\frac{1}{g_0} = \frac{m_r}{2\pi\hbar^2 a} - \frac{1}{V} \sum_{\mathbf{k}} \frac{1}{\epsilon_{B,\mathbf{k}} + \epsilon_{I,\mathbf{k}}}. \quad (7)$$

The variational wavefunction is a superposition of the unscattered impurity at rest $|\mathbf{0}\rangle_I$ immersed in the Bose condensate and the impurity, scattered into momentum state $-\mathbf{k}$, having ejected one boson out of the condensate into momentum \mathbf{k} :

$$|\Psi\rangle = \phi_0 |\mathbf{0}\rangle_I \otimes |\alpha\rangle_B + \sqrt{N_B} \sum_{\mathbf{k}} \phi_{\mathbf{k}} a_{\mathbf{k}}^\dagger |-\mathbf{k}\rangle_I \otimes |\alpha\rangle_B. \quad (8)$$

The factor $\sqrt{N_B}$, where N_B is the average boson number, originates from the destruction operator $a_{\mathbf{0}}$ acting on the condensate, taken to be in a coherent state $|\alpha\rangle_B$ with $\alpha = \sqrt{N_B}$. The expectation values of the kinetic and potential energies are

$$\langle H_0 \rangle = N_B \sum_{\mathbf{k}} |\phi_{\mathbf{k}}|^2 (\epsilon_{B,\mathbf{k}} + \epsilon_{I,\mathbf{k}}) \quad (9)$$

$$\langle V \rangle = g_0 n_B \left(|\phi_0|^2 + \sum_{\mathbf{k}} (\phi_0 \phi_{\mathbf{k}}^* + \phi_0^* \phi_{\mathbf{k}}) + \sum_{\mathbf{k}\mathbf{k}'} \phi_{\mathbf{k}} \phi_{\mathbf{k}'}^* \right) \quad (10)$$

with $n_B = N_B/V$ the boson density. Minimization of the total energy, under the normalization constraint $\langle \Psi | \Psi \rangle = 1$, yields the following set of equations:

$$g_0 n_B \chi = E_p \phi_0 \quad (11)$$

$$g_0 \frac{1}{V} \chi = (E_p - \epsilon_{B,\mathbf{k}} - \epsilon_{I,\mathbf{k}}) \phi_{\mathbf{k}} \quad (12)$$

with $\chi = \phi_0 + \sum_{\mathbf{k}} \phi_{\mathbf{k}}$ and E_p the polaron energy. One thus obtains for the coefficients $\phi_{\mathbf{k}}$:

$$\phi_{\mathbf{k}} = \frac{1}{N_B} \frac{E_p}{E_p - \epsilon_{B,\mathbf{k}} - \epsilon_{I,\mathbf{k}}} \phi_0, \quad (13)$$

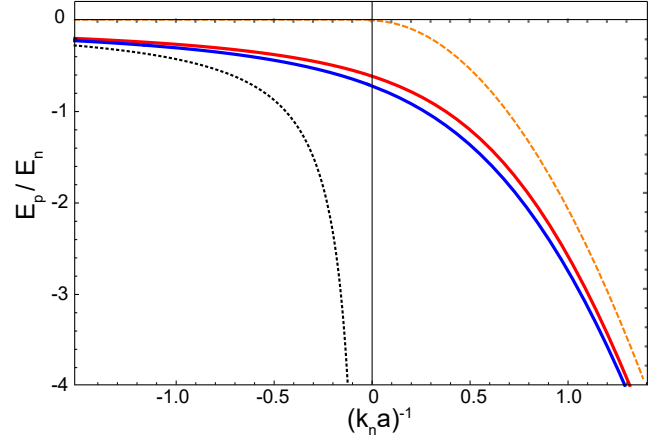


FIG. S4. Binding energy of the Bose and Fermi polaron from the variational ansatz (solid blue and red line, respectively). For comparison, the bare molecular energy is shown (dashed, yellow) as well as the mean-field result (black, dotted).

and for the polaron energy E_p , after eliminating g_0 in favor of the scattering length a :

$$E_p = \frac{n_B}{\frac{m_r}{2\pi\hbar^2 a} - \frac{1}{V} \sum_{\mathbf{k}} \left(\frac{1}{E_p - \epsilon_{B,\mathbf{k}} - \epsilon_{I,\mathbf{k}}} + \frac{1}{\epsilon_{B,\mathbf{k}} + \epsilon_{I,\mathbf{k}}} \right)} \quad (14)$$

Noting that $\frac{1}{V} \sum_{\mathbf{k}} \left(\frac{1}{E_p - \epsilon_{B,\mathbf{k}} - \epsilon_{I,\mathbf{k}}} + \frac{1}{\epsilon_{B,\mathbf{k}} + \epsilon_{I,\mathbf{k}}} \right) = \frac{m_r \kappa}{2\pi\hbar^2}$, where we have set $E_p \equiv -\hbar^2 \kappa^2 / 2m_r$, one obtains the Eq. 1 of the main text:

$$E_p \equiv -\frac{\hbar^2 \kappa^2}{2m_r} = -\frac{2\pi\hbar^2 n_B}{m_r} f(i\kappa) \quad (15)$$

where $f(i\kappa) = -\frac{a}{1-\kappa a}$ is the two-body scattering amplitude at imaginary momentum $i\kappa$. Fig. S4 compares the variational polaron energy of the Bose polaron with that of the Fermi polaron – an impurity immersed in a Fermi sea of the same density. The difference in energies is generally less than $\sim 0.2E_n$ for all interaction strengths. The Fermi polaron is less strongly bound due to the spread of relative momenta in the initial state and Pauli blocking of final scattering states.

The normalization condition $|\phi_0|^2 + N_B \sum_{\mathbf{k}} |\phi_{\mathbf{k}}|^2 = 1$ yields the quasi-particle weight in this approximation:

$$Z \equiv |\phi_0|^2 = \frac{1}{1 + \frac{1}{8\pi} \frac{\kappa^3}{n_B}} = \frac{1}{1 + \frac{1}{2} \left(1 - \frac{E_p}{E_{mf}} \right)} \quad (16)$$

Z is thus simply related to the ratio of E_p and the mean-field result $E_{mf} \equiv \frac{2\pi\hbar^2 n_B a}{m_r}$. On resonance, where $1/E_{mf} = 0$, this approach yields a quasi-particle weight of $Z = 2/3$.

The contact $C \equiv \frac{8\pi m_r}{\hbar^2} \frac{\partial E_p}{\partial (-a^{-1})}$ directly follows from the a -dependence of E_p as

$$\frac{C}{k_n} = \pi^2 \frac{\frac{E_p}{E_n}}{\frac{E_p}{E_n} - \frac{\pi}{4} \frac{1}{k_n a}} \quad (17)$$

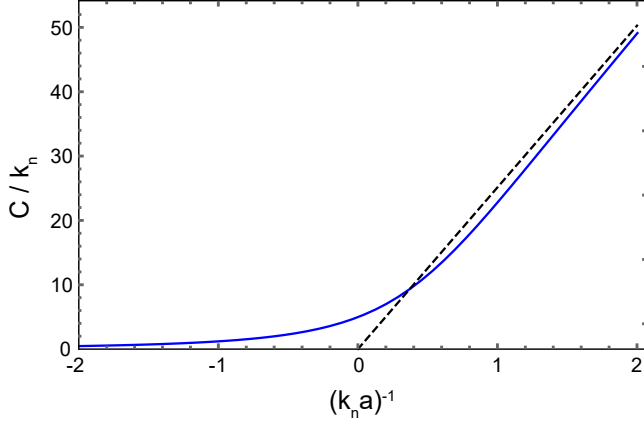


FIG. S5. The contact of the Bose polaron, within the variational ansatz (solid blue). The result for a bare molecule is shown as the dashed black line.

The momentum distribution of the polaron is given by a delta-function centered at $\mathbf{k} = 0$, of weight Z , plus a contribution $n_k = N_B |\phi_k|^2$ from impurity-boson scattering:

$$\begin{aligned} n_k &= \frac{Z}{N_B} \frac{E_p^2}{(E_p - \epsilon_{B,\mathbf{k}} - \epsilon_{I,\mathbf{k}})^2} \\ &= \frac{Z}{N_B} \frac{1}{\left(1 + \frac{k^2}{\kappa^2}\right)^2} \end{aligned} \quad (18)$$

This component of the momentum distribution has the same dependence on momentum as that of a Feshbach molecule of spatial size $1/\kappa$, the length scale set by the polaron energy. In real space, the wavefunction of the polaron thus is a superposition of a delocalized wave of weight Z and a part that is localized, of the form $\frac{1}{r} \exp(-\kappa r)$.

The contact C governs the high-momentum tails of the momentum distribution according to $n_k \rightarrow \frac{C/V}{k^4}$. From that we obtain a relation between the contact, the quasi-particle weight and the polaron energy, valid within this variational approach:

$$\frac{C}{k_n} = \frac{3\pi^2}{2} Z \left(\frac{E_p}{E_n}\right)^2 \quad (19)$$

Rf spectrum of the Bose polaron: Fermi's Golden Rule yields for the radiofrequency spectrum of the Bose polaron:

$$\Gamma_{\text{rf}}(\omega) = \frac{2\pi}{\hbar} \sum_f |\langle f | V_{\text{rf}} | \Psi \rangle|^2 \delta(\hbar\omega - (E_f - E_p)) \quad (20)$$

where $V_{\text{rf}} = \frac{1}{2}\hbar\Omega_R \sum_{\mathbf{k}} d_{\mathbf{k}}^\dagger c_{\mathbf{k}} + \text{c.c.}$, Ω_R is the Rabi frequency, and the sum extends over a complete set of final states $|f\rangle$ of energy E_f . With $d_{\mathbf{k}}^\dagger$ the creation operator for an impurity atom in the final, non-interacting state

of the rf transition, the final states are

$$\begin{aligned} |\mathbf{0}\rangle &\equiv d_0^\dagger |\text{vac}\rangle_I \otimes |\alpha\rangle_B \\ |\mathbf{k}\rangle &\equiv d_{-\mathbf{k}}^\dagger a_{\mathbf{k}}^\dagger |\text{vac}\rangle_I \otimes |\alpha\rangle_B. \end{aligned} \quad (21)$$

where $|\text{vac}\rangle_I$ is the vacuum of the impurity states. The energies of the states $|\mathbf{k}\rangle$ are $E_f = \epsilon_{B,\mathbf{k}} + \epsilon_{I,\mathbf{k}}$. For the coupling matrix elements one has

$$\begin{aligned} \langle \mathbf{0} | V_{\text{rf}} | \Psi \rangle &= \frac{\hbar\Omega_R}{2} \phi_0 \\ \langle \mathbf{k} | V_{\text{rf}} | \Psi \rangle &= \frac{\hbar\Omega_R}{2} \phi_{\mathbf{k}} \alpha \end{aligned} \quad (22)$$

One then finds for the normalized spectrum $\tilde{I}(\omega) \equiv \frac{\Gamma_{\text{rf}}(\omega)E_n}{\frac{\pi}{2}\hbar\Omega_R^2}$:

$$\tilde{I}(\omega) = Z\delta\left(\frac{\hbar\omega}{E_n} + \frac{E_p}{E_n}\right) + \frac{1}{2\pi^2\sqrt{2}} \frac{C}{k_n} \left(\frac{E_n}{\hbar\omega}\right)^2 \sqrt{\frac{\hbar\omega}{E_n} + \frac{E_p}{E_n}} \quad (23)$$

The spectrum has a delta-component shifted by the polaron energy, and a background from impurity-boson scattering that has the same functional form as that of a molecular radiofrequency spectrum [52, 72]. At finite temperature the delta function may be naturally assumed to broaden into a Lorentzian [73]. The variational solution presented here turns out to be identical to the corresponding lowest order T-matrix result [28, 56]. We stress that the inclusion of the non-zero boson-boson interaction strength, contributions from higher-order scattering processes, as well as finite temperature will all act to lower the quasi-particle weight Z further.

Homogeneous properties derived from column-integrated images

For 3D atomic gases, absorption imaging implies line-of-sight (column) integration, resulting in a 2D projection. We derive the local (homogeneous) properties of the Bose polaron from analyzing small regions of this 2D projection. From the impurity absorption images, we obtain the column-integrated impurity transfer, which relates to the local transfer $I^{3D}(\omega, x, y, z)$ via

$$I^{2D}(\omega, y, z) = \frac{\int_{-\infty}^{\infty} dx I^{3D}(\omega, x, y, z) n_K(x, y, z)}{\int_{-\infty}^{\infty} dx n_K(x, y, z)} \quad (24)$$

where the n_K is the impurity density distribution. As we will now discuss, the measured spectral peak, spectral width, and contact are only weakly affected by this column integration. To reconstruct a local rf spectrum from an inhomogeneous sample, one can make use of the line-density-based reconstruction method described in [74, 75]. In brief, $I^{3D}(\omega, x, y, z)$ satisfies LDA and can be written as a function of the local boson chemical potential and rf frequency. In the following, we assume

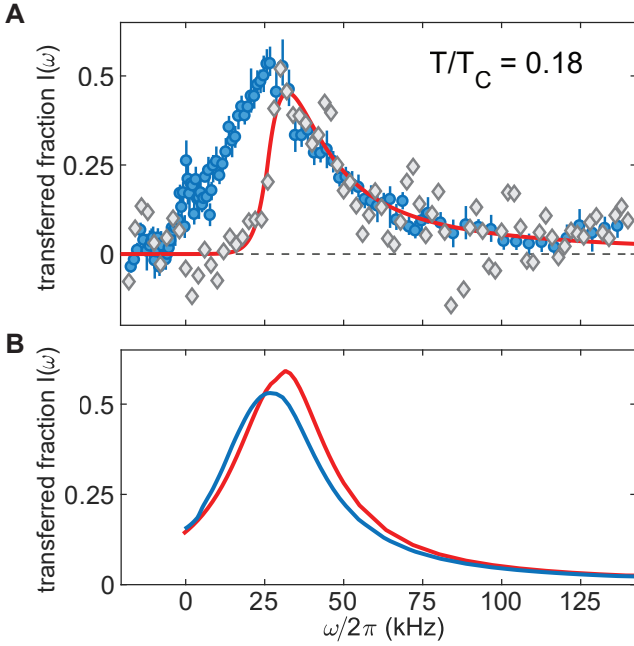


FIG. S6. Effects of column integration on the polaron lineshape. **(A)** The column-integrated rf spectrum (blue circles), as shown in the main text, is compared with the reconstructed local rf spectrum (grey diamonds). The red line is a guide to the eye for the local spectrum. **(B)** The variational prediction of the local rf spectrum, modeled by Eq. 23, is shown as the red line. The blue line is the same spectrum weighted by the spatial impurity distribution and integrated over the x-direction, simulating the column-integrated spectrum in (A).

that the impurities share the same trap geometry as the bosons, a good approximation inside the Thomas-Fermi radius where they experience a strong attractive potential due to the BEC. One can define a one-dimensional impurity transfer

$$I^{1D}(\omega, z) = \frac{1}{n_K^{1D}(z)} \int \int_{-\infty}^{\infty} dx dy I^{3D}(\omega, x, y, z) n_K(x, y, z) \quad (25)$$

where $n_K^{1D}(z)$ is the line density of the impurities. The one-dimensional impurity transfer and the impurity line density can be derived from the absorption images. The local transfer follows the relation [75]

$$I^{3D}(\omega, x=y=0, z) = \frac{d(I^{1D}(\omega, z) n_K^{1D}(z))}{dz} \left(\frac{dn_K^{1D}(z)}{dz} \right)^{-1} \quad (26)$$

Effectively, the local impurity transfer can be recovered from knowledge of the impurity line density and the doubly-integrated impurity transfer, at the cost of performing a numerical derivative. An example of the reconstructed local spectrum is shown in Fig. S6(A) for the axial coordinate $z = \frac{2}{3}R_z$, as well as the spectrum from the corresponding column-integrated data (as shown in the main text). The discrepancy in peak energy shift between the two methods is less than 10%. As expected,

the column-integrated spectrum has a peak shifted toward lower frequencies due to density inhomogeneity. The spectral width of the column-integrated spectrum, as reported in the main text, is defined as the half-width-half-maximum, taking the half width toward high frequencies. This definition of the spectral width avoids including the broadening toward lower frequencies, which is dominated by the contribution from density inhomogeneity. The spectral width obtained from the two methods agree to within the errorbars reported in Fig. 3 of the main text. The local reconstruction method works well near the center of the trap where the bosons and impurities have similar spatial distributions, but fails outside the BEC boundaries where the species-selective optical potential breaks the assumption of identical trap geometry between the bosons and impurities. For this reason, we use the column-integrated transfer and not the reconstructed local transfer $I^{3D}(\omega)$ for all values reported in the main text.

We perform a complementary benchmark of our column-integrated results by numerically simulating a local impurity distribution, using the result from the variational ansatz presented above, with a Lorentzian distribution centered at E_p with full-width-half-maximum γ in place of the delta-function in Eq. 23. Upon column integration and weighted by the impurity's spatial distribution, the local spectrum gives the simulated column-integrated rf spectrum. Here we choose γ as a free parameter to have the best least-squares fit to our column-integrated data. As can be seen in Fig. S6(B), the polaron peak position from the simulated column-integrated spectrum only deviates by approximately 10% of the local binding energy, in agreement with the result from direct reconstruction of the local spectrum.

Linear response

To obtain the contact from the spectral lineshape, we require the rf transfer to be in the linear response regime. Furthermore, the contact's relation to the spectral response (Eq. 2 of the main text) is expected to only hold for the high momentum wings of the cloud, $\hbar\omega \gg E_n$. We extract the contact by fitting the high frequency tail of the ejection spectra where the transfer is well within the linear response regime (below 0.2) and the spectral response follows a $\omega^{-3/2}$ dependence within our signal to noise, as demonstrated in the main text. To confirm that the response is within the linear response regime, we measure the transfer as a function of the rf pulse duration. We verify this linear behavior for various interaction strengths and Rabi frequencies and show one example in Fig. S7(A).

To ensure that our polaron peak and width assignments are not affected by the possible nonlinear response of $I(\omega)$, we measure the spectrum at $a = -3900 a_0$ with varying pulse powers. A comparison of the same spectrum taken with varying peak Rabi frequencies is shown

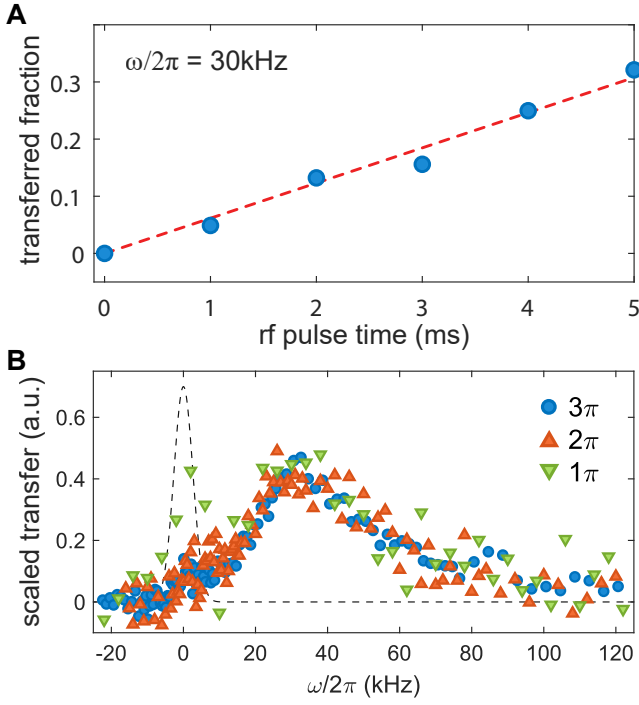


FIG. S7. (A) Time-resolved rf response of the impurity located at the trap center. The interaction strength is $a = -840 a_0$, and a rf pulse with constant power is employed with varying duration at a detuning of $2\pi \times 30$ kHz above the atomic resonance. The dashed line is a linear fit through the data. (B) Rf spectra at $a = -3900 a_0$ and $T/T_c = 0.1$ obtained with Gaussian pulses of varying peak powers, corresponding to a π , 2π , and 3π transfer of the bare atoms from the $|\downarrow\rangle$ to the $|\uparrow\rangle$ state. The three powers are represented by green downward-facing triangles, red upward-facing triangles, and blue circles, respectively.

in Fig. S7(B). The relative heights of the two lower-power spectra have been scaled by arbitrary constants. Neither the assigned peak nor the spectral width are affected beyond the experimental signal-to-noise limitations.